Zhang *et al.*
EURASIP Journal on Advances in Signal Processing (2022) 2022:127
https://doi.org/10.1186/s13634-022-00959-z

EURASIP Journal on Advances in Signal Processing

RESEARCH Open Access

Joint antenna selection and waveform design for coexistence of MIMO radar and communications

Xuan Zhang[1], Xiangrong Wang[1*] and Xianghua Wang[2]

*Correspondence:
xrwang@buaa.edu.cn

[1] School of Electronic and Information Engineering, Beihang University, Xueyuan Road No.37, Beijing, China
[2] School of Artificial Intelligence, Beijing University of Posts and Telecommunications, Xitucheng Road No. 10, Beijing, China

Abstract

As the problem of spectral congestion is becoming severe, the coexistence between two primary spectrum users, radar and communications, has spurred extensive research interest. To reduce the mutual interferences between the two functions, MIMO radar waveform design needs to consider the compatibility in both spectral and spatial domains, where the former is achieved by null forming in the frequency domain and the latter is achieved by shaped beampattern synthesis. Additionally, high power efficiency and low system overhead are two desirable characteristics for MIMO radar system design. To this end, we first introduce a new realistic waveform constraint, peak-to-valley-power-ratio (PVPR) constraint per antenna to improve the power efficiency. Then, combined with PVPR constraint, we propose a switchable individual antenna power control scheme to jointly optimize waveforms and antenna locations. We adopt a max–min beampattern matching criterion and impose the $\ell_{2,\Gamma}$-norm penalty on the waveform matrix to promote the sparsity of the array. To solve the resultant non-smooth and non-convex problem, we develop a modified alternating directions method of multipliers, where a surrogate subproblem over primal variables is solved instead of the original problem, and its local convergence is analyzed. Finally, numerical experiments demonstrate the effectiveness and superiority of the proposed method over counterparts, especially obtaining the lowest sidelobe level and deeper spectral nulls using much fewer antennas.

Keywords: Antenna selection, Coexistence of MIMO radar and communications, Peak-to-valley-power-ratio (PVPR) constraint, Transmit beampattern synthesis, Waveform design

1 Introduction

Recently, the spectrum resources have become increasingly scarce [1–3], and thus collaborative coexistence between radar and communication systems in the spectrally crowed environment has become prominent [4–6]. As a primary bandwidth occupier, the spectral compatibility needs to be considered in the radar waveform design to accommodate other spectral users, such as communications. This can be achieved by forming multiple spectral nulls in the frequency domain of the designed waveforms. As shown in Fig. 1, there are K base stations working in the proximity of MIMO radar

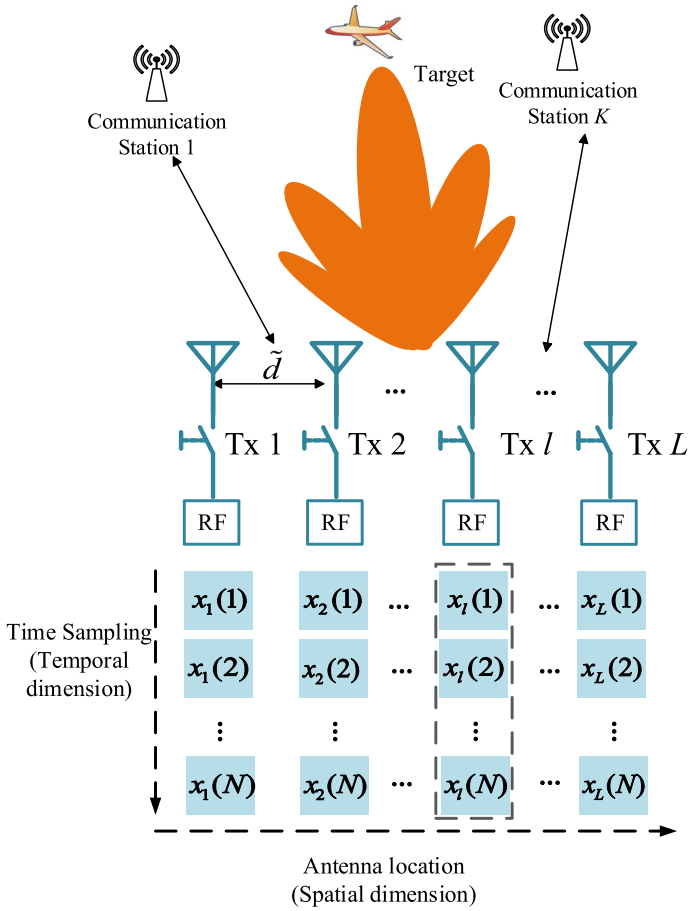

Fig. 1 MIMO array radar with designed waveforms and switchable antennas in coexistence with communications

system, and the base stations share a certain frequency band with radar. In addition to spectral compatibility, the spatial radiation energy produced by MIMO radar in the communication direction should be suppressed to decrease the mutual interferences to communication devices locating within the radar mainlobe. To this end, MIMO radar waveform design should consider both the spectral and spatial compliance for synthesizing a desired energy distribution in the spatial–spectral domain.

In general, the waveform optimization problems for colocated MIMO radar can be classified into the following three categories. The first one considers the joint design of transmit waveforms and receive filters to maximize the output signal-to-interference-plus-noise ratio (SINR) [7–10] in order to mitigate the signal-dependent interference and enhance the target detection probability. The second one studies the transmit beampattern synthesis by concentrating the transmit power on the region of interest while minimizing the power in the other regions [11–18]. The third one is to maximize the mutual information between the target reflections and the target responses [19–21] to improve the detection performance. In our work, we focus on the second one, i.e., transmit beampattern synthesis. Additionally, to overcome the spectral congestion with multiple communication systems, we intend to synthesize spectrally-compatible waveforms with a desired beampattern shape.

There are generally two ways of synthesizing a desired transmit beampattern, indirect way and direct way. The former adopts a two-step process which first optimizes a waveform covariance matrix (WCM) to form a desired beampattern and then performs the probing waveform optimization to approximate the obtained WCM. For example, the authors in [13] proposed to design a desired transmit beampattern by matching an ideal transmit beampattern in square error (SE) sense via using a semidefinite quadratic programming (SDQP) technique to optimize the WCM. Afterward, the literature [14] proposed a cyclic algorithm (CA) to design constant modulus (CM) or low peak-to-average-power ratio (PAR) waveforms to approximate the optimized WCM for obtaining a shaped-good beampattern. In addition, the work in [15] utilized the obtained WCM to synthesize binary-shift keying coded waveforms. Other optimal WCM design methods are also investigated in [16–18]. The latter emphasizes directly optimizing transmit probing waveforms without designing the WCM for a desired transmit beampattern. For instance, the authors in [22] applied the alternating direction method of multipliers (ADMM) [23] to directly synthesize CM waveforms based on the SE-minimization in the beampattern matching criterion. Employing the same matching criterion, [24] solved a quartic optimization problem under the majorization-minimization (MM) framework [25] to design waveforms subject to multiple constraints. Moreover, the work in [26] suppressed the peak sidelobe level (PSL) of the synthesized beampattern with restricted mainlobe ripples. Nevertheless, it is worth stressing that none of the aforementioned works pays attention to the radio frequency (RF) spectrum congestion in the waveform design.

Furthermore, high power efficiency and low system overhead are two desirable characteristics for MIMO radar system design from the viewpoint of practical applications, which are also the cores of this work. To achieve high power efficiency, CM or low PAR constraints are usually imposed on the directly-designed waveform since the radar transmitters only operate in saturation to deliver maximum power efficiency. However, the CM requirement is too strict to improve the performance and it usually is imposed on both temporal and spatial dimension, which may cause an unnecessary loss of degrees of freedom (DoFs). Besides, the PAR constraint has a key shortcoming as explained in [27] that it is insufficient to control the transmit power uniformity across the transmit antennas, which may result in a large power dynamic range and thus reduces the power efficiency. To overcome this issue of PAR constraint, we introduce a more realistic waveform power constraint, referred to as peak-to-valley-power-ratio (PVPR) constraint. The power dynamic range on the transmit waveforms of the lth antenna, $\{x_l(n)\}_{n=1}^{N}$ in Fig. 1, is maintained within an allowable degree of power fluctuation by controlling the value of PVPR. In particular, when PVPR $= 1$, it implies that the waveforms transmitted by the lth antenna satisfy the uniform elemental power requirement, i.e., $|x_l(n)|^2 = \mu_l, \forall n$. Different from CM, various uniform power $\{\mu_l\}_{l=1}^{L}$ can be assigned to the L antennas, which apparently increases more DoFs than the common CM.

To achieve low system overhead, a sparse array (SA) synthesized with MIMO transceiver is further designed via antenna selection, as full MIMO arrays are expensive attributed to the front-end channel associated with each antenna and complicated digital signal processing [28–30]. In addition, SA with an enlarged inter-element spacing can reduce the mutual coupling between antenna elements, specifically at

millimeter wave frequencies with a very small wavelenth [31]. Also, a nonuniform SA with the same number of antennas owns more spatial DoFs brought by configuration flexibility to improve the system performance, such as enhancement of the aperture efficiencies and high resolution in the angular domain [32, 33].

In the recent studies [34–37], the authors investigated the joint optimization on the WCM and antenna position, which is formulated a NP-hard quartic boolean combinational optimization. The convex relaxation methods adopted there usually cannot be guaranteed to be globally optimal. In this paper, different from the existing works, we directly design the probing waveforms circumventing the WCM and the binary selection vector to achieve the array sparsity. Specifically, a $\ell_{2,1}$-norm is imposed on the transmit waveform matrix to promote the group sparsity of the designed waveforms, whose sparse structure indicates the selected antenna positions. Moreover, in light of the fact that each antenna is fed by an individual RF power amplifier (PA), as shown in Fig. 1, it would be pragmatic to control the power uniformity separately on each antenna. Hence, we consider to add a switch to control the connection status of the front end of individual antenna, which is referred to as switchable individual antenna power control (SIAPC). Intuitively, our SIAPC scheme combined with unit-PVPR constraint possess more DoFs than the common CM. Thus, it is expected that the transmit beampattern synthesized by the proposed SIAPC strategy incorporated with PVPR constraint can obtain a lower sidelobe level (SLL) than the existing schemes.

The main contributions of this paper are highlighted as follows:

1 A switchable individual antenna power control (SIAPC) strategy combined with a waveform temporal constraint, peak-to-valley-power-ratio (PVPR), is proposed in this paper to flexibly control the power uniformity per antenna and power distribution across the array. The SIAPC scheme is able to obtain more designate DoFs while using the smallest number of antennas, which thus allows a high power efficiency and low system overhead.
2 To achieve the coexistence of the radar and communications, we propose a max–min criteria to design spectrally-compatible waveforms for shaping desired transmit beampatterns, where the spectral energy nulls are formed in the specified spatial–spectral domain. Meanwhile, a $\ell_{2,1}$-norm penalty term is directly imposed on waveform matrix to promote the group sparsity of the designed waveform. By doing so, we achieve a joint optimization on the antenna positions and transmit waveform.
3 To solve the proposed problem, we develop an efficient method based on a modified alternating directions method of multipliers since the conventional ADMM is hard to tackle such non-convex and non-smooth problem. Specifically, we approximately solve a surrogate subproblem over primal variables such that the non-convex PVPR constraint is solved by a projection operation. We prove that such an approximate solution keeps the original interior monotonicity of the augmented Lagrangian. Numerical experiments verify the effectiveness of the proposed method and improved performance over counterparts.

1.1 Notation

Vectors and matrices are denoted by boldface lowercase and uppercase letters, respectively. The $\|\cdot\|$ denotes the Frobenius norm while $(\cdot)^T$, $(\cdot)^H$, $(\cdot)^*$ and $\angle(\cdot)$ are the transpose, conjugate transpose, complex conjugate and phase operators, respectively. $\Re\{\}$ and $\Im\{\}$ mean the real and imaginary parts of a complex number. $\boldsymbol{I}_n$ denote the identity matrix of size $n \times n$. The symbols $\mathbb{R}$ and $\mathbb{C}$ stand for the complex and real space, respectively. The expression $\lambda_{\max}(\boldsymbol{A})$ means taking the maximum eigenvalue of the matrix $\boldsymbol{A}$.

2 System and signal model

Consider a colocated MIMO radar consisting of a uniform linear array (ULA) of L antennas, as shown in Fig. 1, where two adjacent transmit antennas are equally spaced by $\tilde{d}$. There is one front-end for each antenna, and the connection status of the front-end is controlled by a switch to determine whether it is on or off. Note that the scenario in Fig. 1 enables the detection of targets in the focused main-lobe and simultaneously spectrally coexists with multiple communication users which share certain overlapped frequency bands. Assuming that the discrete-time waveform emitted by the lth antenna is denoted by $x_l(n), n = 1, \ldots, N$, where N denotes the sample number of each radar pulse. Then, we define the waveform vectors along the spatial dimension and the temporal dimension as,

$$\tilde{\boldsymbol{x}}_n = [x_1(n), x_2(n), \ldots, x_L(n)]^T \in \mathbb{C}^{L\times 1}, \tag{1}$$

$$\boldsymbol{x}_l = [x_l(1), x_l(2), \ldots, x_l(N)]^T \in \mathbb{C}^{N\times 1}, \tag{2}$$

and the corresponding concatenated waveform vectors and paralleled matrices are given by,

$$\tilde{\boldsymbol{x}} = [\tilde{\boldsymbol{x}}_1^T, \ldots, \tilde{\boldsymbol{x}}_N^T]^T \in \mathbb{C}^{LN\times 1}, \tilde{\boldsymbol{X}} = [\tilde{\boldsymbol{x}}_1, \ldots, \tilde{\boldsymbol{x}}_N] \in \mathbb{C}^{L\times N}, \tag{3}$$

$$\boldsymbol{x} = [\boldsymbol{x}_1^T, \cdots, \boldsymbol{x}_L^T]^T \in \mathbb{C}^{LN\times 1}, \boldsymbol{X} = [\boldsymbol{x}_1^T; \ldots; \boldsymbol{x}_L^T] \in \mathbb{C}^{L\times N}. \tag{4}$$

Note that there is a relationship between $\tilde{\boldsymbol{x}}$ and $\boldsymbol{x}$, i.e, $\tilde{\boldsymbol{x}} = \boldsymbol{E}\boldsymbol{x}$, where $\boldsymbol{E} = \sum_{l=1}^{L}(\boldsymbol{e}_l^T \otimes \boldsymbol{I}_N \otimes \boldsymbol{e}_l)$ with $\boldsymbol{e}_l \in \mathbb{R}^{L\times 1}$ being a unit-basic vector whose elements are 0 except the lth one is 1. Under the case that the propagation is nondispersive and the transmitted signal is narrow-band, the base-band signal received at the angular direction θ_p is given by [13, 26],

$$\begin{aligned} y &= \sum_{l=1}^{L} e^{j2\pi f_0 \tau_l(\theta_p)} x_l(n) \\ &= \boldsymbol{a}^H(\theta_p)\tilde{\boldsymbol{x}}_n, \end{aligned} \tag{5}$$

where f_0 is the carrier frequency, $\tau_l(\theta_p) = \frac{(l-1)\tilde{d}\sin(\theta_p)}{c}$ with c being the speed of propagation, and $\boldsymbol{a}(\theta_p)$ is the transmit array steering vector defined by,

$$\boldsymbol{a}(\theta_p) = [e^{j2\pi f_0 \tau_1(\theta_p)}, \ldots, e^{j2\pi f_0 \tau_L(\theta_p)}]^T \in \mathbb{C}^{L\times 1}. \tag{6}$$

The transmit beampattern, which describes the cumulated spatial power of the transmitted signal at the direction θ_p, is then given by [13],

$$\begin{aligned} P(\theta_p) &= \sum_{n=1}^{N} |\boldsymbol{a}^H(\theta_p)\tilde{\boldsymbol{x}}_n|^2, \\ &= \|\boldsymbol{A}_{\theta_p}^H \tilde{\boldsymbol{x}}\|_2^2, \\ &= \|\check{\boldsymbol{A}}_{\theta_p}^H \boldsymbol{x}\|_2^2, \end{aligned} \tag{7}$$

where $\check{\boldsymbol{A}}_{\theta_p} = \boldsymbol{E}^T \boldsymbol{A}_{\theta_p}$ with $\boldsymbol{A}_{\theta_p} = \boldsymbol{I}_N \otimes \boldsymbol{a}(\theta_p) \in \mathbb{C}^{LN \times N}$.

For ease of discussion, the spatial angular regions are divided into P uniformly spaced samples, which cover the mainlobe region $\Theta_m = \{\theta_m\}_{m=1}^{M}$ and the sidelobe region $\Theta_s = \{\vartheta_s\}_{s=1}^{S}$. For the MIMO radar transmit beampattern synthesis, a main issue is to design waveform $\boldsymbol{x}$ for shaping a good transmit radiation power distribution on the mainlobe region Θ_m, and the sidelobe region Θ_s. In addition to that, in light of the limitation of the nonlinear PA in the RF circuitry in practical applications, some practical constraints are required to impose on the waveform $\boldsymbol{x}$. For example, the common CM constraint with a fixed amplitude μ_0, i.e.,

$$|x_l(n)| = \mu_0, l = 1, \ldots, L, n = 1, \ldots, N, \tag{8}$$

is usually imposed on $\boldsymbol{x}$ to maximize the transmit power efficiency. Usually, the relaxed PAR constraint [14, 38], i.e.,

$$\mathrm{PAR}(\boldsymbol{x}_l) = \frac{\max_n |x_l(n)|^2}{\frac{1}{N}\sum_{n=1}^{N} |x_l(n)|^2} \leq \delta, \tag{9}$$

where $\delta \in [1, N]$, is employed instead of the rigorous CM constraint. Unfortunately, as revealed in [27, 39], Eq (9) accompanied with the per-antenna energy constraint (EC), i.e., $\|\boldsymbol{x}_l\|^2 = \frac{\kappa_e^2}{L}$ is equivalent to,

$$|x_l(n)|^2 \leq \tilde{\kappa}_e, l = 1, \ldots, L, n = 1, \ldots, N, \tag{10}$$

where $\tilde{\kappa}_e = \frac{\delta \kappa_e^2}{NL}$ with κ_e^2 being the total energy budget. From (10), we see that PAR constraint has a major drawback that there may exist a large dynamic power fluctuation for the lth transmit antenna in the N samples since no lower bound is imposed on (10). Note that this drawback is not beneficial to the maximization of the transmission power efficiency. To fill this gap, we introduce a realistic power constraint into waveform design, referred to as peak-to-valley-power ratio (PVPR) constraint, which can control the power uniformity of each transmit antenna for improving the power efficiency.

2.1 Per-antenna PVPR constraint

We define the waveform PVPR constraint on the lth antenna as,

$$\mathrm{PVPR}(x_l) = \frac{\max_{n=1,\ldots,N} |x_l(n)|^2}{\min_{n=1,\ldots,N} |x_l(n)|^2} \leq \sigma_l, \tag{11}$$

which restricts the ratio of the maximum power to the minimum one over N samples emitted by the lth antenna less than a preset threshold σ_l, so as to control the difference of transmit power among the N samples per antenna. Here, σ_l plays a role of controlling the power uniformity among N samples for the lth transmit antenna and different σ_l for $l = 1, \ldots, L$ can be assigned to control the varying power uniformity on L antennas. Regarding the PVPR constraint (11), we discuss some points as follows:

1 ***Remark 1***

Since the RF amplifier for each front antenna feed is individual per Fig. 1, it is feasible and beneficial to incorporate the PVPR constraint into switchable individual antenna power control (SIAPC). Intuitively, the combination of PVPR and SIAPC can decrease the system cost while creating more designate DoFs to improve the performance of radar systems, such as lowering the beampattern sidelobe level.

1 ***Remark 2***

The PVPR constraint is actually a general power control constraint. As when we set $\sigma_l = 1$ *in (11), it degenerates to unit-PVPR constraint, i.e.,*

$$|x_l(n)| = \sqrt{\mu_l}, n = 1, \ldots, N, \forall l. \tag{12}$$

Note that μ_l is a scaling factor to be optimized. This is different from the conventional CM constraint (8), which constrains the uniformity in both temporal and spatial dimensions, while the unit-PVPR relaxes the spatial dimension and focuses on elemental uniformity, thus earning more designate DoFs. On the other hand, when the PVPR constraint is imposed on both spatial dimension and temporal dimension, i.e.,

$$\mathrm{PVPR}(x) = \frac{\max_{l,n=1,\ldots,L,N} |x_l(n)|^2}{\min_{l,n=1,\ldots,L,N} |x_l(n)|^2} \leq \sigma_0, \tag{13}$$

the unit-PVPR constraint in (13) with $\sigma_0 = 1$ under the total energy constraint, i.e., $\|\boldsymbol{x}\|^2 = \kappa_e^2$ coincides with the CM constraint, i.e.,

$$|x_l(n)| = \frac{\kappa_e}{\sqrt{NL}}, \forall n, l. \tag{14}$$

This manifests the generality of the proposed PVPR constraint.

2.2 Spectral coexistence with communications

In a spectrally crowed scenario, the radar system is required to coexist with communication devices while simultaneously detecting the targets of interest [39–43]. In this respect, we desire that the synthesized radar waveforms are not only able to focus energy in the spatial direction of targets but also to suppress mutual interferences on overlaid communication services, especially those in the mainlobe. To this end, we assume that there are K communication devices and each of them operates on a frequency band $\Omega_k = [f_{k,1}, f_{k,2}]$ for $k = 1, \ldots, K$, where $f_{k,1}$ and $f_{k,2}$ are the

lower and upper normalized frequencies for the kth device, respectively. Besides, we suppose that the kth communication device is located on the spatial angle range $\tilde{\Phi}_k = [\vartheta_{k,1}^c, \vartheta_{k,2}^c]$. Then, the integrated energy on the kth communication in the specific space-frequency region is given by [42],

$$\begin{aligned} E_k &= \int_{\vartheta_{k,1}^c}^{\vartheta_{k,2}^c} \int_{f_{k,1}}^{f_{k,2}} \bar{D}(\theta, f) \mathrm{d}f \, \mathrm{d}\vartheta \\ &= \tilde{\boldsymbol{x}}^H (\boldsymbol{F}_k \otimes \boldsymbol{U}_k) \tilde{\boldsymbol{x}} \\ &= \boldsymbol{x}^H \boldsymbol{\Omega}_k \boldsymbol{x} \end{aligned} \tag{15}$$

where $\bar{D}(\theta, f)$ denotes the Energy Spectral Density (ESD), $\boldsymbol{\Omega}_k = \boldsymbol{E}^T (\boldsymbol{F}_k \otimes \boldsymbol{U}_k) \boldsymbol{E}$ with $\boldsymbol{F}_k \in \mathbb{C}^{N \times N}$ and $\boldsymbol{U}_k \in \mathbb{C}^{L \times L}$ being the frequency matrix and angle matrix of the kth space-frequency region, respectively, which are defined by [40–42],

$$\boldsymbol{F}_k(n_1, n_2) = \begin{cases} f_{k,2} - f_{k,1}, & n_1 = n_2 \\ \frac{e^{j2\pi f_{k,2}(n_1 - n_2)} - e^{j2\pi f_{k,1}(n_1 - n_2)}}{j2\pi(n_1 - n_2)}, & n_1 \neq n_2 \end{cases} \tag{16}$$

and

$$\begin{aligned} \boldsymbol{U}_k(l_1, l_2) &= \int_{\vartheta_{k,1}^c}^{\vartheta_{k,2}^c} e^{-j(l_1 - l_2) \frac{2\pi f_0 \tilde{d} \sin\vartheta}{c}} \mathrm{d}\vartheta \\ &= \begin{cases} \sin\vartheta_{k,2}^c - \sin\vartheta_{k,1}^c, & l_1 = l_2 \\ \frac{e^{j\pi \sin\vartheta_{k,2}^c (l_1 - l_2)} - e^{j\pi \sin\vartheta_{k,1}^c (l_1 - l_2)}}{j\pi(l_1 - l_2)}, & l_1 \neq l_2 \end{cases} \end{aligned}$$

Accordingly, the total energy produced on the all K communication devices is given by,

$$\begin{aligned} E_s(\boldsymbol{x}) &= \sum_{k=1}^{K} \boldsymbol{x}^H \tilde{\boldsymbol{\Omega}}_k \boldsymbol{x}, \\ &= \boldsymbol{x}^H \boldsymbol{\Omega} \boldsymbol{x}, \end{aligned} \tag{17}$$

where $\boldsymbol{\Omega} = \sum_{k=1}^{K} \boldsymbol{\Omega}_k$.

To facilitate the MIMO radar in spectral coexistence with communications, it is desirable to minimize the total energy E_s in order to reduce mutual interferences to other communication devices. In the ensuing section, we will incorporate the PVPR constraint (11) into the waveform optimization which involves the transmit beampattern synthesis and spectral coexistence with communications.

2.3 Problem formulation

For the radar operation, it usually desires to concentrate the radiation power in the mainlobe region while lowering the power level in the sidelobes [13, 17, 44] for sake of target detection and radar clutter/jamming suppression. To this end, we propose a min-max design under PVPR constraint to fully explore the DoFs for suppressing the sidelobes and shaping the mainlobe while introducing a $\ell_{2,1}$-norm regularizer to promote the waveform group sparsity so as to achieve antenna selection. More precisely,

our goal is to minimize the maximum matching error between the synthesized beampattern $P(\theta_p)$ and the desired one D_p subject to PVPR constraint, which is formulated as the following optimization problem,

$$\begin{aligned} &\min_{\boldsymbol{x}} \ \max_{p} \left\{ w_p \left| \|\check{\boldsymbol{A}}_{\theta_p}^H \boldsymbol{x}\|_2^2 - D_p \right| \right\}_{p=1}^P + \tau \|\boldsymbol{X}\|_{2,1} + \beta E_s(\boldsymbol{x}) \\ &\text{s.t. } \mathrm{PVPR}(\boldsymbol{x}_l) \le \sigma_l, l \in \mathbb{S}, \end{aligned} \tag{18}$$

where w_p for $p = 1, \ldots, P$ are the weight coefficients that emphasize different certain angular region over others, $\tau > 0$ is the regularization parameter that compromises between the beampattern shape and the sparsity on antennas, β represents the penalty parameter on the spectral energy suppression, and $\mathbb{S}$ denotes the support set containing the indices of nonzero waveform vectors in the set $\{\boldsymbol{x}_l\}_{l=1}^L$.

1 ***Remark 3***

In the proposed design, we do not consider the waveform total energy constraint, i.e., $\|\boldsymbol{x}\|^2 = \kappa_e^2$. *The reason is that once we obtain the solution, e.g.,* $\boldsymbol{x}^\star$, *we can normalize* $\boldsymbol{x}^\star$ *as* $\boldsymbol{x}_o = \frac{\kappa_e \boldsymbol{x}^\star}{\|\boldsymbol{x}^\star\|_2}$ *to meet the constraint* $\|\boldsymbol{x}\|^2 = \kappa_e^2$. *Notice that such a scaled* $\boldsymbol{x}_o$ *does not affect the PVPR constraint, neither the beampattern shape, as well as the relative spectral energy distribution under the normalization processing.*

1 ***Remark 4***

Note that problem (17) is very challenging to solve. The difficulties are that the objective functions are non-smooth attributed to the discontinuous function $\max\{\cdot\}$ *and particularly contain the inseparable quadratic terms* $\|\check{\boldsymbol{A}}_{\theta_p}^H \boldsymbol{x}\|_2^2$ *in* $\boldsymbol{x}_l$, *which makes the per-antenna PVPR constraint on* $\boldsymbol{x}_l$ *hard to tackle. To deal with this issue, we resort to a splitting method to solve the resultant problem as in the next section.*

3 Proposed method

In this section, we derive an efficient algorithm via modifying the standard ADMM framework to solve the formulated problem in (17). Specifically, since solving (17) directly is very difficult due to the existence of the discontinuous function $\max\{\cdot\}$, we first introduce an auxiliary variable η to rephrase (17) as,

$$\begin{aligned} &\min_{\boldsymbol{x}_l} \ \eta + \tau \sum_{l=1}^{L} \|\boldsymbol{x}_l\|_2 + \beta \boldsymbol{x}^H \boldsymbol{\Omega} \boldsymbol{x} \\ &\quad \text{s.t. } \left| \|\boldsymbol{A}_p^H \boldsymbol{x}\|_2^2 - D_p \right| \le \frac{\eta}{w_p}, p = 1, \ldots, P, \\ &\quad \mathrm{PVPR}(\boldsymbol{x}_l) \le \sigma_l, l \in \mathbb{S}, \end{aligned} \tag{19}$$

where $\boldsymbol{A}_p = \check{\boldsymbol{A}}_{\theta_p}$ for notional brevity.

Furthermore, (18) is equivalent to,

$$\begin{aligned} &\min_{\boldsymbol{x},\eta} \ \eta + \tau \sum_{l=1}^{L} \|\boldsymbol{x}_l\|_2 + \beta \boldsymbol{x}^H \boldsymbol{\Omega} \boldsymbol{x} \\ &\text{s.t. } D_p - \frac{\eta}{w_p} \le \|\boldsymbol{A}_p^H \boldsymbol{x}\|_2^2 \le D_p + \frac{\eta}{w_p}, p = 1, \ldots, P, \\ &\text{PVPR}(\boldsymbol{x}_l) \le \sigma_l, l \in \mathbb{S}, \end{aligned} \tag{20}$$

By defining $\hat{\boldsymbol{A}}_p = \sqrt{w_p}\boldsymbol{A}_p$, we continue to simplify (19) as,

$$\begin{aligned} &\min_{\boldsymbol{x},\eta} \ \eta + \tau \sum_{l=1}^{L} \|\boldsymbol{x}_l\|_2 + \beta \boldsymbol{x}^H \boldsymbol{\Omega} \boldsymbol{x} \\ &\text{s.t. } D_p w_p - \eta \le \|\hat{\boldsymbol{A}}_p^H \boldsymbol{x}\|_2^2 \le D_p w_p + \eta, p = 1, \ldots, P, \\ &\text{PVPR}(\boldsymbol{x}_l) \le \sigma_l, l \in \mathbb{S}. \end{aligned} \tag{21a}$$

Note that (20) is still difficult to handle as η is coupled in the lower and upper bounds, which makes (20) intractable. To solve (20), we again introduce an auxiliary variable $\boldsymbol{\nu}_p$ and impose the equality constraints, i.e., $\hat{\boldsymbol{A}}_p^H \boldsymbol{x} = \boldsymbol{\nu}_p$ for $p = 1, \ldots, P$ on (20), yielding the following equivalent problem,

$$\begin{aligned} &\min_{\boldsymbol{x},\boldsymbol{\nu}_p,\eta} \ \eta + \tau \sum_{l=1}^{L} \|\boldsymbol{x}_l\|_2 + \beta \boldsymbol{x}^H \boldsymbol{\Omega} \boldsymbol{x} \\ &\text{s.t. } \hat{\boldsymbol{A}}_p^H \boldsymbol{x} = \boldsymbol{\nu}_p, p = 1, \ldots, P, \end{aligned} \tag{21b}$$

$$d_p - \eta \le \|\boldsymbol{\nu}_p\|_2^2 \le d_p + \eta, p = 1, \ldots, P, \tag{21c}$$

$$\text{PVPR}(\boldsymbol{x}_l) \le \sigma_l, l \in \mathbb{S}, \tag{22}$$

where $d_p = D_p w_p$. From (21), we can see that the constraints $d_p - \eta \le \|\boldsymbol{\nu}_p\|^2 \le d_p + \eta$ and $\text{PVPR}(\boldsymbol{x}_l) \le \sigma_l$ will act their roles in respective subproblems with respect to (w.r.t) variables $\boldsymbol{\nu}_p$ and $\boldsymbol{x}_l$, respectively. However, $\boldsymbol{\nu}_p$ and $\boldsymbol{x}$ are coupled together in the additional constraint (21a). This variable splitting characteristic enables us to utilize the ADMM strategy for solving (21). Specifically, we first construct the augmented Lagrangian function of (21) in terms of (21a) as,

$$\begin{aligned} \mathcal{L}_\rho(\boldsymbol{x}, \eta, \boldsymbol{\nu}_p, \tilde{\boldsymbol{u}}_p) = \eta + \tau \sum_{l=1}^{L} \|\boldsymbol{x}_l\|_2 + \beta \boldsymbol{x}^H \boldsymbol{\Omega} \boldsymbol{x} \\ + \sum_{p=1}^{P} \Re\{\tilde{\boldsymbol{u}}_p^H (\hat{\boldsymbol{A}}_p^H \boldsymbol{x} - \boldsymbol{\nu}_p)\} + \frac{\rho}{2} \sum_{p=1}^{P} \|\hat{\boldsymbol{A}}_p^H \boldsymbol{x} - \boldsymbol{\nu}_p\|^2, \end{aligned} \tag{23}$$

where $\rho > 0$ is the penalty parameter and $\{\tilde{\boldsymbol{u}}_p\}_{p=1}^P$ are dual variables. By introducing the scaled dual variable $\boldsymbol{u}_p = \frac{\tilde{\boldsymbol{u}}_p}{\rho}$, we can recast (22) as,

$$\begin{aligned}\mathcal{L}_\rho(\boldsymbol{x},\eta,\boldsymbol{v}_p,\boldsymbol{u}_p) = \eta + \tau\sum_{l=1}^{L}\|\boldsymbol{x}_l\|_2 + \beta\boldsymbol{x}^H\boldsymbol{\Omega}\boldsymbol{x} \\ + \frac{\rho}{2}\sum_{p=1}^{P}(\|\hat{\boldsymbol{A}}_p^H\boldsymbol{x} - \boldsymbol{v}_p + \boldsymbol{u}_p\|^2 - \|\boldsymbol{u}_p\|^2).\end{aligned} \tag{24}$$

It follows the ADMM alternates minimizing the augmented Lagrangian function $\mathcal{L}_\rho$ w.r.t $\boldsymbol{x}$ and $\boldsymbol{v}_p$ along with the dual ascent update on $\boldsymbol{u}_p$ to produce the following iteration steps:

$$\begin{aligned}&\text{Step1}: \boldsymbol{x}^{t+1} = \underset{\boldsymbol{x}}{\operatorname{argmin}}\ \mathcal{L}_\rho(\boldsymbol{x},\eta^t,\boldsymbol{v}_p^t,\boldsymbol{u}_p^t),\\ &\quad \text{s.t. PVPR}(\boldsymbol{x}_l) \le \sigma_l, l \in \mathbb{S};\end{aligned} \tag{25}$$

$$\begin{aligned}&\text{Step2}: \{\boldsymbol{v}_p^{t+1},\eta^{t+1}\} = \underset{\boldsymbol{v}_p}{\operatorname{argmin}}\ \mathcal{L}_\rho(\boldsymbol{x}^{t+1},\eta,\boldsymbol{v}_p,\boldsymbol{u}_p^t)\\ &\text{s.t. } d_p - \eta \le \|\boldsymbol{v}_p\|_2^2 \le d_p + \eta, p = 1,\ldots,P;\end{aligned} \tag{26}$$

$$\text{Step3}: \boldsymbol{u}_p^{t+1} = \boldsymbol{u}_p^t + \hat{\boldsymbol{A}}_p^H\boldsymbol{x}^{t+1} - \boldsymbol{v}_p^{t+1}, \tag{27}$$

where t denotes the count of iterations.

In what follows, we discuss the solutions to the subproblems (24) and (25), respectively.

1) The solution to (24): The $\boldsymbol{x}$-subproblem in (24) by omitting the irrelative items, is given by,

$$\begin{aligned}&\min_{\boldsymbol{x}}\ \sum_{p=1}^{P}\|\hat{\boldsymbol{A}}_p^H\boldsymbol{x} - \boldsymbol{z}_p\|^2 + \frac{2\tau}{\rho}\sum_{l=1}^{L}\|\boldsymbol{x}_l\|_2 + \frac{2\beta}{\rho}\boldsymbol{x}^H\boldsymbol{\Omega}\boldsymbol{x}\\ &\quad \text{s.t. PVPR}(\boldsymbol{x}_l) \le \sigma_l, l \in \mathbb{S},\end{aligned} \tag{28}$$

where $\boldsymbol{z}_p = \boldsymbol{v}_p^t - \boldsymbol{u}_p^t$. To clearly solve (27), we further simplify (27) as,

$$\begin{aligned}&\min_{\boldsymbol{x}}\ \boldsymbol{x}^H\boldsymbol{B}\boldsymbol{x} - 2\Re\{\boldsymbol{x}^H\boldsymbol{b}\} + \frac{2\tau}{\rho}\sum_{l=1}^{L}\|\boldsymbol{x}_l\|_2\\ &\quad \text{s.t. PVPR}(\boldsymbol{x}_l) \le \sigma_l, l \in \mathbb{S},\end{aligned} \tag{29}$$

where $\boldsymbol{B} = \sum_{p=1}^{P}\hat{\boldsymbol{A}}_p\hat{\boldsymbol{A}}_p^H + \frac{2\beta}{\rho}\boldsymbol{\Omega}$ and $\boldsymbol{b} = \sum_{p=1}^{P}\hat{\boldsymbol{A}}_p\boldsymbol{z}_p$.

However, we find that the quadratic term $\boldsymbol{x}^H\boldsymbol{B}\boldsymbol{x}$ in (28) is inseparable for $\boldsymbol{x}_l, l = 1,\ldots,L$, which makes the update of $\boldsymbol{x}_l^{t+1}$ subject to PVPR constraint complicated. To this end, we propose to update $\boldsymbol{x}_l^{t+1}$ in an approximated manner. More specifically, we first introduce the following *Lemma 1* to help us seek a simpler surrogate problem for (28).

Lemma 1 [45]: *Let $\boldsymbol{L}$ be $N \times N$ Hermitian matrix and $\boldsymbol{M}$ be another $N \times N$ Hermitian matrix such that $\boldsymbol{M} \succeq \boldsymbol{L}$. Then, for any point $\boldsymbol{x}^t \in \mathbb{C}^{N\times 1}$, the quadratic function $\boldsymbol{x}^H\boldsymbol{L}\boldsymbol{x}$ is majorized by*:

$$\begin{aligned} \boldsymbol{x}^H \boldsymbol{L}\boldsymbol{x} \leq\ & \boldsymbol{x}^H \boldsymbol{M}\boldsymbol{x} + 2\Re\{\boldsymbol{x}^H(\boldsymbol{L}-\boldsymbol{M})\boldsymbol{x}^t\} \\ & + \boldsymbol{x}^{(t)H}(\boldsymbol{M}-\boldsymbol{L})\boldsymbol{x}^t. \end{aligned} \tag{30}$$

According to *Lemma 1*, we define $\boldsymbol{L} = \boldsymbol{B}$ and $\boldsymbol{M} = \delta \boldsymbol{I}$ with $\delta = \lambda_{\max}(\boldsymbol{B})$ and linearize the quadratic term $\boldsymbol{x}^H \boldsymbol{B}\boldsymbol{x}$ as its a local upper bound function $g(\boldsymbol{x}, \boldsymbol{x}^t)$ at $\boldsymbol{x}^t$, i.e.,

$$\begin{aligned} \boldsymbol{x}^H \boldsymbol{B}\boldsymbol{x} \leq\ & g(\boldsymbol{x}, \boldsymbol{x}^t) \\ =\ & \delta \|\boldsymbol{x}\|_2^2 + 2\Re\{\boldsymbol{x}^H \boldsymbol{R}\boldsymbol{x}^t\} - \boldsymbol{x}^{(t)H}\boldsymbol{R}\boldsymbol{x}^t, \end{aligned} \tag{31}$$

where $\boldsymbol{R} = \boldsymbol{B} - \delta \boldsymbol{I}_{NL}$.

It is worth stressing that differing from the original ADMM strategy that directly solves the problem (28), our scheme is to update $\boldsymbol{x}^{t+1}$ by replacing $\boldsymbol{x}^H \boldsymbol{B}\boldsymbol{x}$ with $g(\boldsymbol{x}, \boldsymbol{x}^t)$ in (28) and ignoring the constant terms, which results in the following surrogate problem,

$$\begin{aligned} & \min_{\boldsymbol{x}}\ \delta \|\boldsymbol{x}\|_2^2 - 2\Re\{\boldsymbol{x}^H(\boldsymbol{b} - \boldsymbol{R}\boldsymbol{x}^t)\} + \tau \sum_{l=1}^{L} \|\boldsymbol{x}_l\|_2 \\ \Rightarrow\ & \min_{\boldsymbol{x}}\ \delta \sum_{l=1}^{L} \|\boldsymbol{x}_l - \boldsymbol{y}_l\|^2 + \frac{2\tau}{\rho} \sum_{l=1}^{L} \|\boldsymbol{x}_l\|_2 \\ & \text{s.t. } \mathrm{PVPR}(\boldsymbol{x}_l) \leq \sigma_l, l \in \mathbb{S}, \end{aligned} \tag{32}$$

where $\boldsymbol{y}_l$ is the lth subvector of $\boldsymbol{y} = [\boldsymbol{y}_1^T, \ldots, \boldsymbol{y}_L^T]^T$ defined by,

$$\boldsymbol{y} = \frac{1}{\delta}(\boldsymbol{b} - \boldsymbol{R}\boldsymbol{x}^t) = \boldsymbol{x}^t - \frac{1}{\delta}(\boldsymbol{B}\boldsymbol{x}^t - \boldsymbol{b}). \tag{33}$$

It is obvious that such a transformation in (31) makes the objective function become separable in $\boldsymbol{x}_l$ for $l = 1, \ldots, L$ and much easier to solve $\boldsymbol{x}_l$ constrained in the PVPR constraint. Specifically, the lth subproblem of (31) is given by,

$$\begin{aligned} & \min_{\boldsymbol{x}_l}\ \frac{2\tau}{\rho}\|\boldsymbol{x}_l\|_2 + \delta \|\boldsymbol{x}_l - \boldsymbol{y}_l\|^2 \\ & \text{s.t. } \mathrm{PVPR}(\boldsymbol{x}_l) \leq \sigma_l, l \in \mathbb{S}. \end{aligned} \tag{34}$$

Note that the PVPR constraint in (33) depends on the support set $\mathbb{S}$, which is explicitly related to the sparsity-inducing term $\tau \sum_{l=1}^{L} \|\boldsymbol{x}_l\|_2$. Hence, we have to first determine the support set $\mathbb{S}$. To this end, regardless of the PVPR constraint, we find that the unconstrained optimization (33) admits a closed-form solution as given by the block soft thresholding formula:

$$\boldsymbol{x}_l = \begin{cases} \boldsymbol{q}_l, & \text{if } \|\boldsymbol{y}_l\|_2 \geq \hat{\tau} \\ \boldsymbol{0}_N, & \text{if } \|\boldsymbol{y}_l\|_2 < \hat{\tau} \end{cases} \tag{35}$$

where $\boldsymbol{q}_l = (1 - \frac{\hat{\tau}}{\|\boldsymbol{y}_l\|_2})\boldsymbol{y}_l$ with $\hat{\tau} = \frac{\tau}{\rho\delta}$. From (34), we can naturally obtain the support set $\mathbb{S}$ as,

$$\mathbb{S} = \{l | \|\boldsymbol{y}_l\|_2 \geq \hat{\tau}\}, \tag{36}$$

and under its complementary set $\mathbb{N} = \{l | \|\boldsymbol{y}_l\|_2 < \hat{\tau}\}$, we accordingly set $\boldsymbol{x}_l, l \in \mathbb{N}$ as zero vector, i.e., $\mathbf{0}_N$. For $\boldsymbol{x}_l, l \in \mathbb{S}$, we turn to solve the following projection problem as,

$$\begin{aligned} &\min_{\boldsymbol{x}_l} \ \|\boldsymbol{x}_l - \boldsymbol{q}_l\|^2 \\ &\text{s.t. } \mathrm{PVPR}(\boldsymbol{x}_l) \le \sigma_l. \end{aligned} \tag{37}$$

It can be seen that (36) is intractable due to the non-convex PVPR constraint. To facilitate solving (36), we tactfully introduce a scalar μ to equivalently rewrite (36) as,

$$\begin{aligned} &\min_{\mathbf{x}_l, \mu} \ \|\mathbf{x}_l - \mathbf{q}_l\|_2^2 \\ &\text{s.t. } \mu \le |x_l(n)|^2 \le \mu\sigma_l, n = 1, \ldots, N. \end{aligned} \tag{38}$$

By defining $\zeta = \sqrt{\mu}$ and $\nu_l = \sqrt{\sigma_l}$, we find that (37) is equivalent to,

$$\begin{aligned} &\min_{\mathbf{x}_l, \zeta} \ \|\mathbf{x}_l - \mathbf{q}_l\|_2^2 \\ &\text{s.t. } \zeta \le |x_l(n)| \le \zeta \nu_l, n = 1, \ldots, N. \end{aligned} \tag{39}$$

Fortunately, the solution to (38) admits a closed-form solution ζ_o, which can be determined by the technique in [46]. After obtaining ζ_o, we then have the optimal $\mu^\star = \zeta_o^2$ and each element of $\boldsymbol{x}_l^{t+1}, l \in \mathbb{S}$ can be updated by the following projection:

$$x_l^{t+1}(n) = \begin{cases} \mu^\star \sigma_l e^{j\angle q_l(n)}, & |q_l(n)|^2 \ge \mu^\star \sigma_l \\ \mu^\star e^{j\angle q_l(n)}, & |q_l(n)|^2 \le \mu^\star \\ q_l(n), & \text{otherwise} \end{cases} \tag{40}$$

for $n = 1, \ldots, N$. Once obtaining the solution $\boldsymbol{x}_l^{t+1}$ for both cases of $l \in \mathbb{S}$ or not, then the concatenated vector $\boldsymbol{x}^{t+1}$ is constructed by $\boldsymbol{x}^{t+1} = [\boldsymbol{x}_1^{(t+1)T}, \ldots, \boldsymbol{x}_L^{(t+1)T}]^T$.

Note that when the common CM constraint (8) is considered in $\boldsymbol{x}$-subproblem with $\tau = 0$, the optimal $\boldsymbol{x}^{t+1}$ is readily updated by an element-wise manner as $\boldsymbol{x}^{t+1} = [\mu_0 e^{\angle y(1)}, \ldots, \mu_0 e^{\angle y(NL)}]^T$.

2) The solution to (25): The $\boldsymbol{v}_p$-subproblem in (25) by omitting the irrelative items, is given by,

$$\begin{aligned} &\min_{\boldsymbol{v}_p, \eta > 0} \ \eta + \frac{\rho}{2} \sum_{p=1}^{P} \|\boldsymbol{v}_p - \tilde{\boldsymbol{v}}_p\|^2 \\ &\text{s.t. } d_p - \eta \le \|\boldsymbol{v}_p\|^2 \le d_p + \eta, p = 1, \ldots, P, \end{aligned} \tag{41}$$

where $\tilde{\boldsymbol{v}}_p = \hat{\boldsymbol{A}}_p^H \boldsymbol{x}^{t+1} + \boldsymbol{u}_p^t$. Clearly, once given η, $\boldsymbol{v}_p^{t+1}$ can be updated by solving the following problem,

$$\begin{aligned} &\min_{\boldsymbol{v}_p} \ \sum_{p=1}^{P} \|\boldsymbol{v}_p - \tilde{\boldsymbol{v}}_p\|^2 \\ &\text{s.t. } d_p - \eta \le \|\boldsymbol{v}_p\|^2 \le d_p + \eta, p = 1, \ldots, P, \end{aligned} \tag{42}$$

which admits a closed-form solution as,

$$\boldsymbol{\nu}_p^{t+1} = \begin{cases} \sqrt{d_p+\eta}\,\frac{\tilde{\boldsymbol{\nu}}_p}{\|\tilde{\boldsymbol{\nu}}_p\|_2}, & \|\tilde{\boldsymbol{\nu}}_p\|_2 \geq \sqrt{d_p+\eta} \\ \sqrt{d_p-\eta}\,\frac{\tilde{\boldsymbol{\nu}}_p}{\|\tilde{\boldsymbol{\nu}}_p\|_2}, & \|\tilde{\boldsymbol{\nu}}_p\|_2 \leq \sqrt{d_p-\eta} \\ \tilde{\boldsymbol{\nu}}_p, & \text{otherwise} \end{cases} \tag{43}$$

Then, plugging (42) into the cost function in (40) yields an optimization problem only in terms of η:

$$\begin{aligned} &\min_{\eta}\ \eta + \frac{\rho}{2}\sum_{p=1}^{P}\mathcal{G}(\tilde{\boldsymbol{\nu}}_p)\big|_{\eta\leq\|\tilde{\boldsymbol{\nu}}_p\|^2-d_p}\left(\sqrt{d_p+\eta}-\|\tilde{\boldsymbol{\nu}}_p\|_2\right)^2 \\ &+\frac{\rho}{2}\sum_{p=1}^{P}\mathcal{G}(\tilde{\boldsymbol{\nu}}_p)\big|_{\eta\leq d_p-\|\tilde{\boldsymbol{\nu}}_p\|^2}\left(\sqrt{d_p-\eta}-\|\tilde{\boldsymbol{\nu}}_p\|_2\right)^2, \\ &\text{s.t. } \eta\in[0,\check{\eta}], \end{aligned} \tag{44}$$

where $\check{\eta} = \max_p\{d_p\}_{p=1}^P$ and $\mathcal{G}(\cdot)|_{\mathcal{C}}$ denote the condition function that equals 1 if the argument satisfies $\mathcal{C}$ and equals 0 otherwise. It can be seen that the objective function in (43) is a piecewise nonlinear one that relies on the value of the condition function $\mathcal{G}(\cdot)|_{\mathcal{C}}$. To this end, we select J reasonable and non-overlapped turning points that are less than $\check{\eta}$ from the set $\left\{\left|\|\tilde{\boldsymbol{\nu}}_p\|^2-d_p\right|\right\}_{p=1}^P$ and sort them as $\{\check{r}_j\}_{j=1}^J$ in ascending order, which naturally divides the feasible domain of η into $J+1$ subintervals. Evidently, the optimal solution $\eta^\star$ to (43) corresponds to the smallest one among the objective values in the $J+1$ subintervals. Therefore, we first study the local minimum in each subinterval. Specifically, at the jth subinterval, i.e., $\eta\in[\check{r}_{j-1},\check{r}_j]$, the subproblem of (43) is given by,

$$\begin{aligned} &\min_{\eta}\ \bar{a}_j\eta - \rho\sum_{p=1}^{P}\mathcal{G}(\tilde{\boldsymbol{\nu}}_p)\big|_{\eta\leq\|\tilde{\boldsymbol{\nu}}_p\|^2-d_p}\left(\|\tilde{\boldsymbol{\nu}}_p\|_2\sqrt{d_p+\eta}\right) \\ &-\rho\sum_{p=1}^{P}\mathcal{G}(\tilde{\boldsymbol{\nu}}_p)|_{\eta\leq d_p-\|\tilde{\boldsymbol{\nu}}_p\|^2}\left(\|\tilde{\boldsymbol{\nu}}_p\|_2\sqrt{d_p-\eta}\right)+\bar{c}_j \\ &\text{s.t. } \eta\in[\check{r}_{j-1},\check{r}_j], \end{aligned} \tag{45}$$

where

$$\begin{aligned} \bar{a}_j &= 1+\frac{\rho}{2}\sum_{p=1}^{P}\mathcal{G}(\tilde{\boldsymbol{\nu}}_p)\big|_{\eta\leq\|\tilde{\boldsymbol{\nu}}_p\|^2-d_p} - \frac{\rho}{2}\sum_{p=1}^{P}\mathcal{G}(\tilde{\boldsymbol{\nu}}_p)|_{\eta\leq d_p-\|\tilde{\boldsymbol{\nu}}_p\|^2}, \\ \bar{c}_j &= \frac{\rho}{2}\sum_{p=1}^{P}\mathcal{G}(\tilde{\boldsymbol{\nu}}_p)\big|_{\eta\leq\|\tilde{\boldsymbol{\nu}}_p\|^2-d_p}\left(d_p+\|\tilde{\boldsymbol{\nu}}_p\|_2^2\right) \\ &\quad+\frac{\rho}{2}\sum_{p=1}^{P}\mathcal{G}(\tilde{\boldsymbol{\nu}}_p)|_{\eta\leq d_p-\|\tilde{\boldsymbol{\nu}}_p\|^2}\left(d_p+\|\tilde{\boldsymbol{\nu}}_p\|_2^2\right). \end{aligned} \tag{46}$$

Denote the cost function in (44) as $f_j(\eta)$ and its first-order derivative and the second-order derivative are given by, respectively,

$$
\begin{aligned}
f_j'(\eta) &= \bar{a}_j - \sum_{p=1}^{P} \mathcal{G}(\tilde{\boldsymbol{\nu}}_p)\big|_{\eta \le \|\tilde{\boldsymbol{\nu}}_p\|^2 - d_p} \frac{\rho \|\tilde{\boldsymbol{\nu}}_p\|_2}{2\sqrt{d_p + \eta}} \\
&\quad + \sum_{p=1}^{P} \mathcal{G}(\tilde{\boldsymbol{\nu}}_p)|_{\eta \le d_p - \|\tilde{\boldsymbol{\nu}}_p\|^2} \frac{\rho \|\tilde{\boldsymbol{\nu}}_p\|_2}{2\sqrt{d_p - \eta}}, \\
f_j''(\eta) &= \sum_{p=1}^{P} \mathcal{G}(\tilde{\boldsymbol{\nu}}_p)\big|_{\eta \le \|\tilde{\boldsymbol{\nu}}_p\|^2 - d_p} \frac{\rho \|\tilde{\boldsymbol{\nu}}_p\|_2}{4(d_p + \eta)^{\frac{3}{2}}} \\
&\quad + \sum_{p=1}^{P} \mathcal{G}(\tilde{\boldsymbol{\nu}}_p)|_{\eta \le d_p - \|\tilde{\boldsymbol{\nu}}_p\|^2} \frac{\rho \|\tilde{\boldsymbol{\nu}}_p\|_2}{4(d_p - \eta)^{\frac{3}{2}}}.
\end{aligned} \tag{47}
$$

Clearly, $f'(\eta)$ is increasing over η and $f''(\eta) > 0$, which implies that the subfunction $f_j(\eta)$ is convex. Thus, the local optimal solution to the jth subproblem in $\eta \in [\check{r}_{j-1}, \check{r}_j]$ can be determined from one of the following three cases:

(1) When $f'(\check{r}_{j-1}) > 0$, the subfunction $f_j(\eta)$ is increasing in the interval $[\check{r}_{j-1}, \check{r}_j]$ and the local minimizer $\hat{\eta}_j = \check{r}_{j-1}$.
(2) When $f'(\check{r}_j) < 0$, the subfunction $f_j(\eta)$ is decreasing in the interval $[\check{r}_{j-1}, \check{r}_j]$ and the local minimizer $\hat{\eta}_j = \check{r}_j$.
(3) When $f'(\check{r}_{j-1}) < 0$ and $f'(\check{r}_j) > 0$, there exists a unique solution to $f_j(\eta)$ in the interval $[\check{r}_{j-1}, \check{r}_j]$ and the local minimizer $\hat{\eta}_j$ can be obtained by applying a bisection search to the equation $f'(\eta) = 0$ in the interval $[\check{r}_{j-1}, \check{r}_j]$.

After obtaining $\hat{\eta}_j$ and its objective value $f_j(\hat{\eta}_j)$ for $j = 1, \ldots, J$, we then choose the smallest one from $\{f_j(\hat{\eta}_j)\}_{j=1}^{J}$ and set the corresponding $\hat{\eta}_j$ as the optimal $\eta^\star$, that is the update of η^{t+1}. Once getting η^{t+1}, $\boldsymbol{\nu}_p^{t+1}$ can be updated by inserting η^{t+1} into (42).

Finally, we summarize the above steps in Algorithm 1 and repeat it until the maximum iteration number T_m is reached or the maximum residual, i.e., $\max_p \|\hat{\boldsymbol{A}}_p^H \boldsymbol{x}^t - \boldsymbol{\nu}_p^t\|_2$ is less than the stop tolerance value ε.

Algorithm 1 : The solution to (17)

Input: antenna number L, sample size N, iteration termination tolerance ε and the maximum iteration number T_m.
Initialization: set $\{\mathbf{u}_p^0\}_{p=1}^P$ and $\{\mathbf{v}_p^0\}_{p=1}^P$;
while $\|\eta^{t+1} - \eta^t\|_2 \le \varepsilon$ and $t \le T_m$
  Update $\mathbf{x}^{t+1}$ by solving the PVPR projection (31);
  Update $\{\mathbf{v}_p^{t+1}, \eta^{t+1}\}$ by solving (42) and (44);
  Update $\mathbf{u}_p^{t+1}$ by (26);
end
Output: MIMO radar waveform $\mathbf{x}^\star = \mathbf{x}^{t+1}$.

4 Performance analysis

4.1 Computational complexity analysis

As for the computational complexity of the proposed Algorithm 1, we mainly consider the count of multiplications in each iteration. In Step1, the maximum eigenvalue of $\boldsymbol{B}$

can be pre-computed before the iteration to save the computational burden. Hence, the main computation in Step1 is involved in the matrix–vector multiplication $\boldsymbol{B}\boldsymbol{x}^t$ which takes $\mathcal{O}(N^2L^2)$ complexity, since the PVPR projection only needs scalar multiplications with the complexity of $\mathcal{O}(NL)$. Step2 is dominated by the matrix–vector multiplications similar to the Step3 with a complexity of $\mathcal{O}(N^2PL)$, as updating η^{t+1} also only needs scalar multiplications. In summary, the overall complexity of Algorithm 1 is $\mathcal{O}(2N^2PL + N^2L^2)$.

4.2 Convergence analysis

In the proposed ADMM-based Algorithm 1, we approximately update $\boldsymbol{x}^{t+1}$ by solving surrogate primal variable subproblems, which actually follows the majorization-minimization algorithm at one step [25]. Note that such a solution by this way can be guaranteed to make the original objective function value decent at each successive update and the proof can be found in [25, 45]. Thus, the interior monotonicity of the original augmented Lagrangian function $\mathcal{L}_\rho(\boldsymbol{x}, \eta^{t+1}, \boldsymbol{v}_p^{t+1}, \boldsymbol{u}_p^t)$ is also guaranteed. Then, we apply some convergence results of the standard ADMM in [23, 47, 48] to study the local convergence of Algorithm 1 and show that $\|\boldsymbol{x}^{t+1} - \boldsymbol{x}^t\|^2 \to 0$ as the iteration number $t \to \infty$. The following theorem is provided to explain the convergence behavior of Algorithm 1 under some mild conditions.

Theorem 1 *Let* $\{\boldsymbol{x}^t, \eta^t, \boldsymbol{v}_p^t, \boldsymbol{u}_p^t\}$ *be the sequence generated by the proposed Algorithm* 1. *Assume that* $\lim_{t\to\infty} \boldsymbol{u}_p^{t+1} - \boldsymbol{u}_p^t = \boldsymbol{0}$ *for* $\forall p$. *Then there exists an accumulation point* $\{\boldsymbol{x}^\star, \eta^\star, \boldsymbol{v}_p^\star, \boldsymbol{u}_p^\star\}$, *which is an optimal solution to* (21).

1 ***Proof***

see Appendix A.

5 Numerical results

In this section, some numerical examples are provided to demonstrate the superiority of the proposed SIAPC scheme over the counterparts. In the first subsection, we examine Algorithm 1 to jointly design waveforms and SA for approaching desired transmit beampatterns $\{D_p\}_{p=1}^P$ without considering compatibility, that is, $\beta = 0$. In the second subsection, we take the spectral energy regularization into account and investigate the coexistence performance of radar and communications. Without loss of generality, we set $\sigma_l = \sigma, \forall l$ to control the power uniformity per antenna with the total energy budget $\kappa_e^2 = NL$. Besides, in all simulations, we set $T_m = 10^4, \varepsilon = 10^{-5}$ in the proposed algorithm and the range of spatial angle is divided into 181 grid points with a uniform interval of 1°.

5.1 Waveform design based on SA without spectral compatibility

1 ***Example 1***

In the first example, a SA is selected from a full ULA consisting of $L = 15$ *antennas with an inter-element spacing of half-wavelength and* $N = 10$ *samples of transmit waveform is designed to synthesize multiple narrow beams, where three beams pointing toward* $\Theta_m = [-50°, 0°, 50°]$ *and the sidelobe region is* $\Theta_s = [-90°, -60°] \cup [-40°, -10°] \cup [10°, 40°] \cup [60°, 90°]$. *We carry out the proposed Algorithm 1 with* $\rho = 0.5, \tau = 0.2$ *and weights* $w_p = 1, \forall p$ *under the random initializations of* $\boldsymbol{x}^0$ *and* $\{\boldsymbol{v}_p^0\}_{p=1}^P$. *Figure 2 illustrates the convergence performance of Algorithm 1 under* $\sigma = 1, 2$, *where the objective* η *steadily converges to a certain point while the maximal residual* $\max_p \|\hat{\boldsymbol{A}}_p^H \boldsymbol{x}^t - \boldsymbol{v}_p^t\|_2$ *decreases to zero, e.g., around -150 dB as the iteration number increases. This indicates the convergence of the proposed method. Also, as expected, a larger PVPR value results in a smaller* η *thanks to more DoFs gained. Figure 3a depicts the synthesized beampatterns using different methods and their corresponding SA configurations are shown in Fig. 3b. The recent WCM-based SA design methods, such as dynamic programming (DP) in [35] and the preset array reconfigured method in [36] (simplified as DP-WCM and RM-WCM, respectively) are performed with 10 antennas selected for fair comparison without cross-correlation term. Meanwhile, a 10-antenna ULA based on optimal WCM design via semi-definite quadratic programming (SQP) method [13] is included for comparison. We can see that the synthesized beampatterns from the SA optimized by our scheme with unit-PVPR has a lower SLL compared to the other methods and outperforms the uniform ULA, which demonstrates the superiority of nonuniform SA over uniform array with the same number of antennas. Moreover, the maximal square error (MSE), defined by* $\text{MSE} = \max_p |\mathcal{B}(\theta_p) - D_p|^2$, *and the PSL are listed in Table 1, which shows that SIAPC scheme exhibits the smallest MSE and the lowest PSL.*

To clearly visualize the optimized waveforms by our SIAPC scheme, the normalized amplitude distributions of the designed waveforms are depicted in Fig. 4a–b. It can be observed that the proposed PVPR constraint enables to control the amplitude dynamic range on each antenna within an acceptable fluctuation, which is beneficial to the individual PA working in a nonlinear region for improving power efficiency. Furthermore, in Fig. 5, we compare the obtained beampattern by SA with unit-PVPR to that of the 15-antenna ULA based on the optimal WCM by SQP and CM waveform. Interestingly, the optimized SA by SIAPC scheme with unit-PVPR exhibits slightly lower SLL than that of full ULA under CM waveform and their MSEs in order are −20.0 dB, −26.96 dB

Table 1 Comparisons of performance in Example 1

Metric	ULA-SQP	RM-WCM	DP-WCM	SA: unit-PVPR	SA: PVPR≤ 2
MSE (dB)	− 13.31	− 9.99	− 18.63	− 27.44	− 27.54
PSL (dB)	− 10.84	− 9.61	− 10.91	− 13.72	− 13.77

Table 2 Comparisons of performance in Example 2

Metric	ULA-SQP	RM-WCM	DP-WCM	SA: unit-PVPR	SA: PVPR≤ 2
MSE (dB)	− 5.77	− 9.23	− 6.56	− 25.11	− 25.13
PSL (dB)	− 8.69	− 9.78	− 8.66	− 12.57	− 12.57

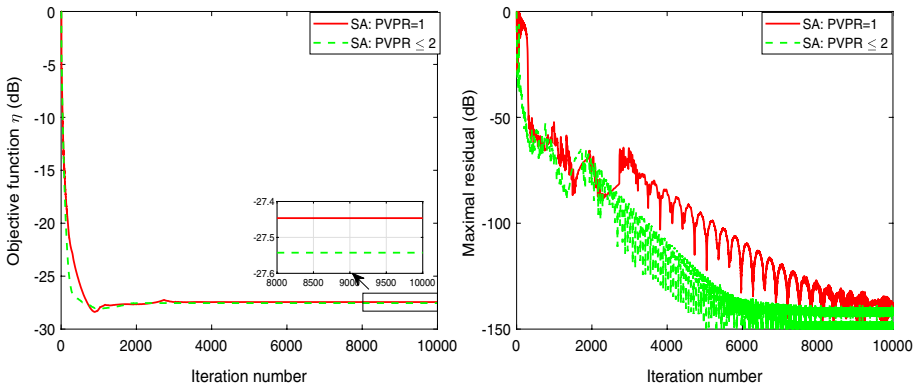

(a) (b)

Fig. 2 **a** the objective function η versus iteration number; **b** the maximal residual $\max_p \|\hat{\boldsymbol{A}}_p^H \boldsymbol{x}^t - \boldsymbol{v}_p^t\|_2$ versus iteration number

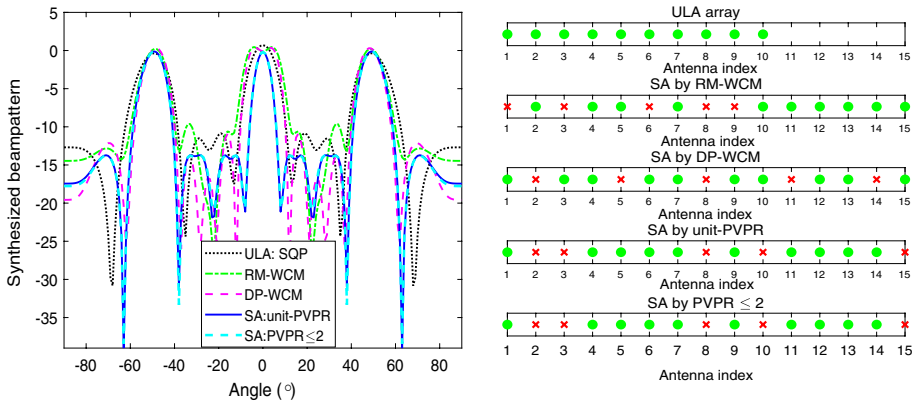

(a) (b)

Fig. 3 **a** Synthesized focused beampatterns with different methods; **b** Antenna locations, where red crosses denote the discarded antennas and green solid circles the selected antennas

and −27.44 dB. Clearly, our SIAPC achieves the best beampattern matching design, i.e., MSE=−27.44 dB.

Finally, to verify the rationality and credibility of the selected antenna locations, we exhaustively search all antenna selection combinations of choosing 10 elements from the full 15-element array with the optimized waveform by the proposed SA method under unit-PVPR constraint. Figure 6 shows that the PSL of the synthesized beampatterns corresponding to all 3003 combinations. We can see that the proposed antenna location shown in Fig. 4a is globally optimal with the lowest PSL.

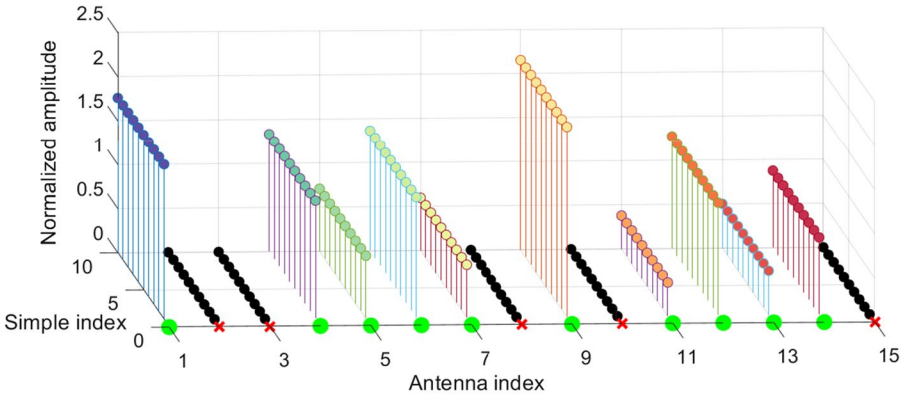

(a) SIAPC with PVPR=1

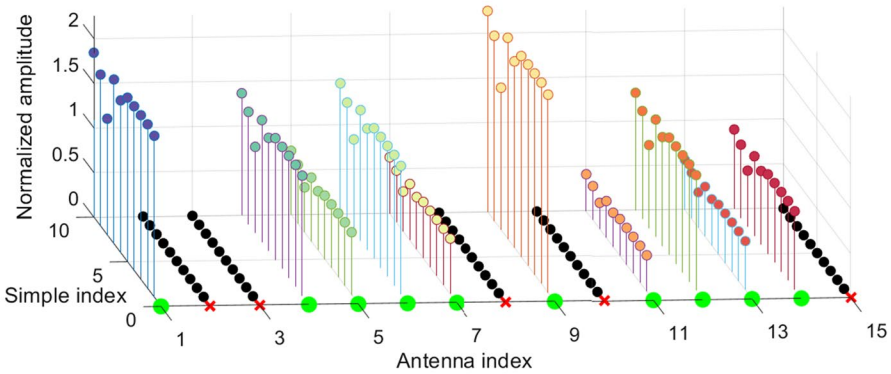

(b) SIAPC with PVPR≤ 2

Fig. 4 Normalized transmit waveform amplitude distribution

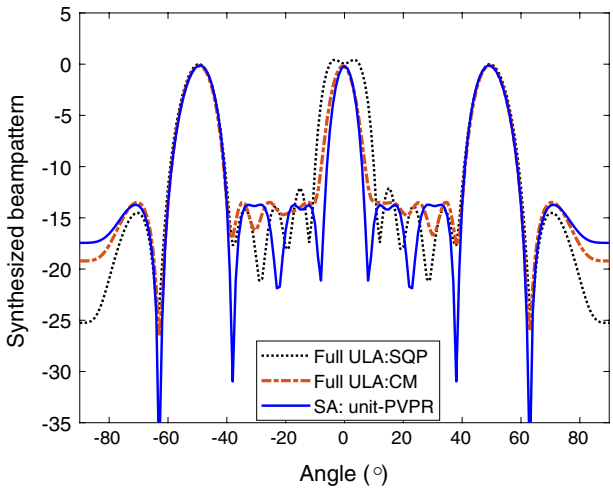

Fig. 5 Focused beampattern comparison of the proposed SA with the full ULA

1 *Example 2*

In the second example, we consider synthesizing multiple wide beams to track multiple potential targets, whereas the directions of the true targets are imprecisely known [49]. To

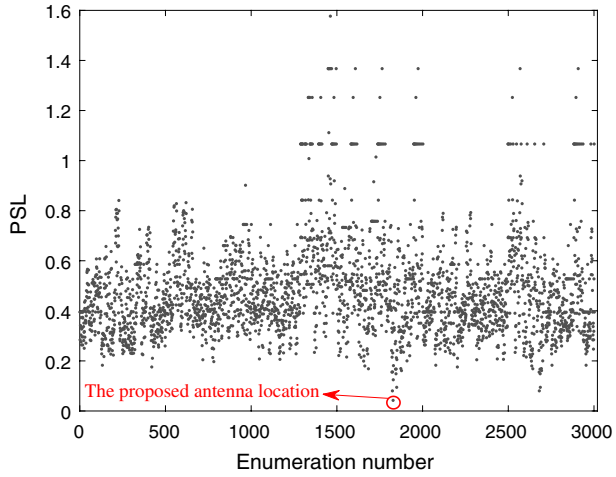

Fig. 6 The PSL of the synthesized beampattern under unit-PVPR constraint versus enumeration number in example 1

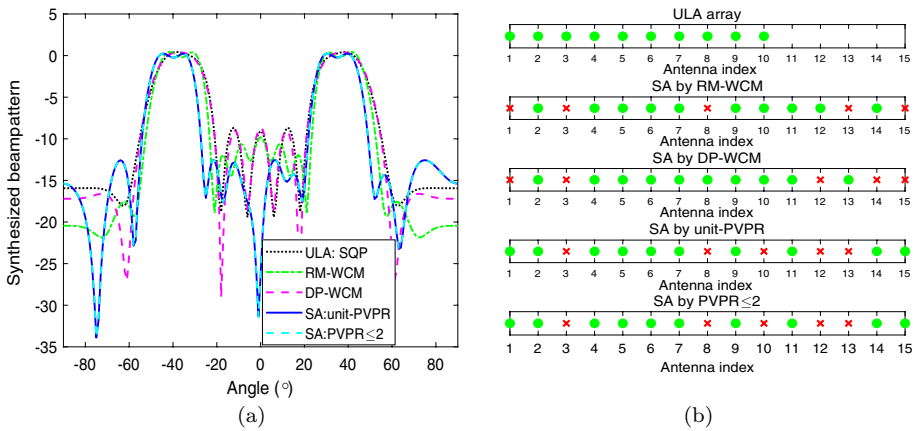

(a) (b)

Fig. 7 **a** Synthesized wide-mainlobe beampatterns with different methods; **b** Antenna locations, where red crosses denote the discarded antennas and green solid circles the selected antennas

this end, we intend to design a two-mainlobe beampattern from a full 15-antenna ULA, where the mainlobe region is $\Theta_m = [-47°, -33°] \cup [28°, 42°]$ *and the sidelobe region is* $\Theta_s = [-90°, -55°] \cup [-25°, 20°] \cup [50°, 90°]$. *Figure 7 displays the synthesized beampatterns of different methods and their selected antenna positions. It can be observed that the designed beampattern from the optimized SA by our SIAPC scheme exhibits the lowest SLL with the same 10 antennas selected. Again, Table 2 shows that the proposed SIAPC utilizes more DoFs to synthesize the beampattern with the smallest MSE and the lowest PSL. Moreover, we also compare the beampattern synthesized by the optimized SA with unit-PVPR to that of the full ULA in Fig. 8. This figure shows that the proposed SIAPC scheme is able to achieve almost the same performance with a full ULA but employing a smaller number of antennas in the beampattern synthesis.*

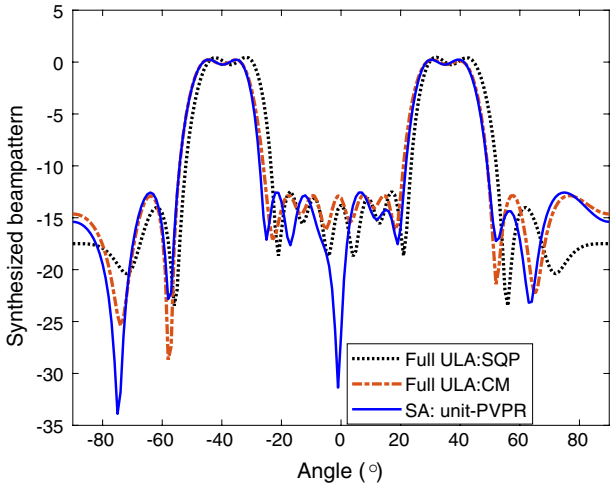

Fig. 8 Wide-mainlobe beampattern comparison of the proposed SA with the full ULA

5.2 Waveform design based on SA with spectral compatibility

1 *Example 3*

In the second part, we further investigate wide beam synthesis but with spectral compatibility, where a full ULA with $L = 15$ *antennas spaced by half-wavelength is constructed and* $N = 32$ *waveform samples is jointly designed. Assume that there are two communication devices spectrally coexisting with the MIMO radar on the normalized working frequency bands* $\Omega_1 = [0.41, 0.51]$ *and* $\Omega_2 = [0.75, 0.85]$. *The two devices are approximately located at the angular positions of* $[-15°, -10°]$ *and* $[10°, 15°]$, *respectively. The desired transmit beampattern for MIMO radar detects targets from the mainlobe region of* $\Theta_m = [-15°, 15°]$ *and the sidelobe region is* $\Theta_s = [-90°, -25°] \cup [25°, 90°]$. *Evidently, the radar detection beam produces large energy leakage in the spatial-spectral directions of communications, which interferes the coexistence between radar and communications. To achieve the spectral coexistence between radar and communications, we set* $\rho = 0.7, \tau = 0.1$ *and* $\beta = 100$ *in Algorithm 1 to synthesize spectrally-compliant beampatterns under different array configurations as shown in Fig. 9a, b, where the performances of the 10-antenna ULA and the 15-antenna full ULA are compared with the proposed SA design. From the figures, we can see the synthesized beampattern under the proposed SA configuration with PVPR=1 exhibits lower PSL than that of the 10-antenna ULA with CM constraint, i.e.,* -18.03 *dB* < -16.13 *dB. Furthermore, the obtained PSL from the proposed SA scheme is slightly larger than that of the full ULA, i.e.,* -18.03 *dB* > -18.4 *dB but requires 5 fewer antennas. In addition, we find that the resulting beampattern of the SA by the proposed SIAPC scheme with PVPR*≤ 2 *exhibits a lower PSL than that of the full ULA, i.e.,* -19.32 *dB* < -18.4 *dB, which again demonstrates the superiority of the proposed strategy.*

The energy distributions of the designed waveforms in the spatial-spectral domain are depicted in Fig. 10, where the yellow rectangular box denotes the spatial-spectral

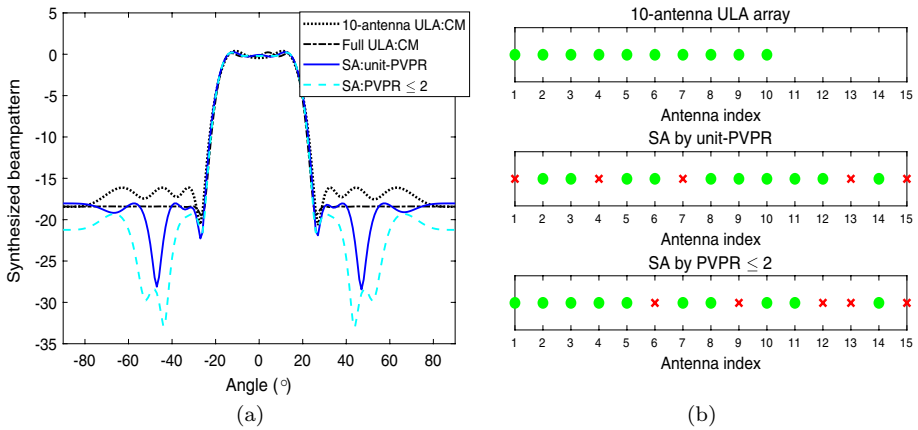

(a) (b)

Fig. 9 **a** Synthesized beampatterns with spectral compatibility; **b** Antenna locations

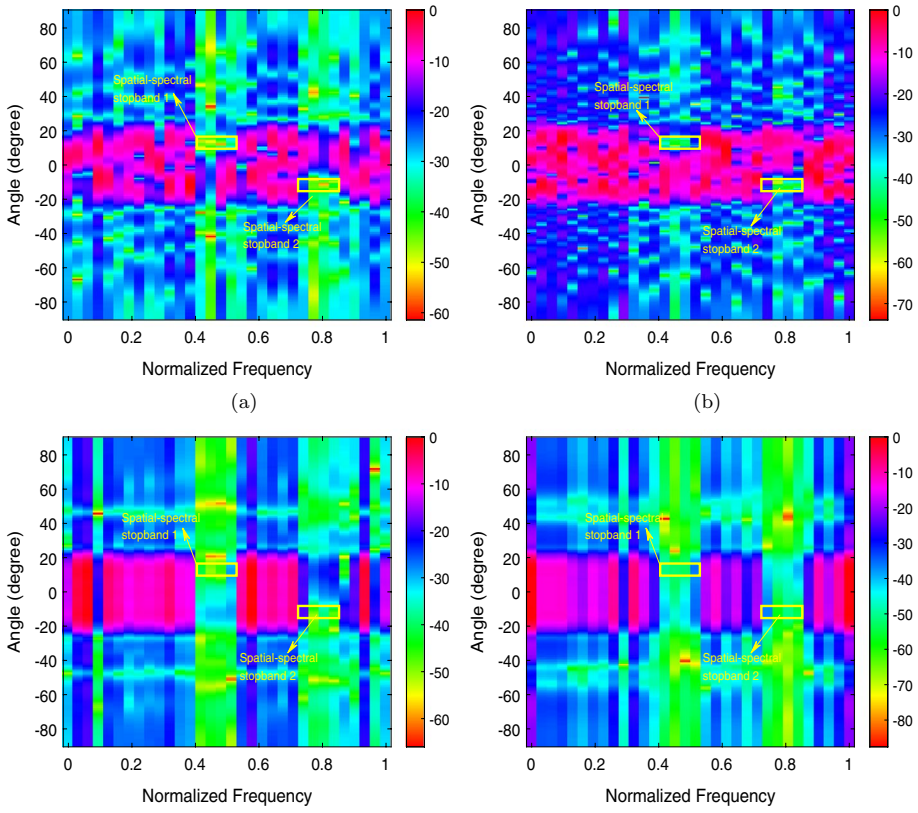

(a) (b) (c) (d)

Fig. 10 The energy distributions in the spatial–spectral domain with $\beta = 100$ under different array configurations. **a** 10-antenna ULA with CM. **b** full ULA with CM. **c** SA with PVPR=1. **d** SA with PVPR≤ 2

stop-bands to be formed. As expected, all the optimized waveforms form deep spectral nulls in the stop-bands, which locally approaches $-$ 50 dB. In particular, it can be observed from Fig. 10c that the optimized waveform by our SIAPC scheme under PVPR=1 forms a more pronounced spectral stop-band stripe than those ULAs in the

CM case in Fig. 10a, b, which is attributed to the more DoFs provided by the PVPR constraint than the CM constraint.

1 *Example 4*

Finally, we examine the ability of the designed waveform to achieve the spectral compatibility with communications when the communication devices locate quite close to the radar target directions. Assume that there are two targets of interest at the angular locations of $-20°$ *and* $10°$*, respectively. Thereby, two focused beams need to be synthesized to probe them with the mainlobe region being* $\Theta_m = [-21°, 19°] \cup [9°, 11°]$ *and the sidelobe region being* $\Theta_s = [-90°, -29°] \cup [-11°, 1°] \cup [19°, 90°]$*. Two communication devices locate very close to the target directions at the angular ranges of* $[-15°, -10°]$ *and* $[10°, 15°]$*, respectively, and their normalized working frequency bands are* $\Omega_1 = [0.30, 0.35]$ *and* $\Omega_2 = [0.80, 0.87]$*. We select 10 antennas from a full 15-antenna array by carrying out the proposed Algorithm 1 with* $\rho = 0.7, \tau = 0.5$ *and* $\beta = 50$*. Figure 11a shows that the synthesized beampatterns under different array configurations. We can see that the beampattern from the proposed SA with unit-PVPR has the smallest PSL of* $-$ *17.23 dB, especially lower than that of the full array. Figure 11b shows that the*

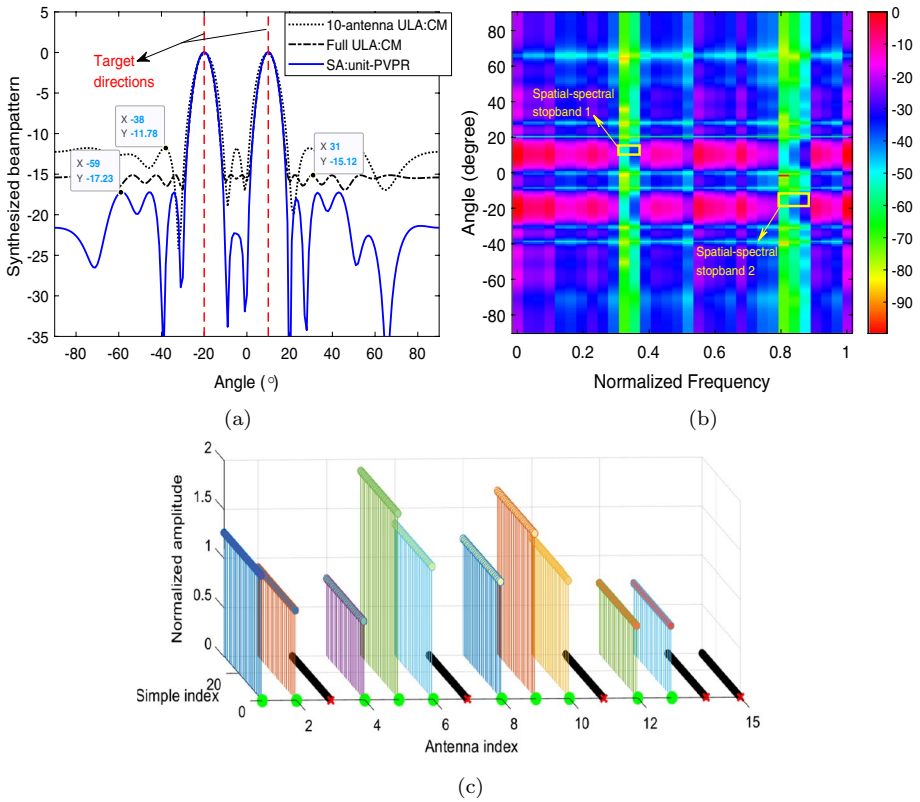

Fig. 11 **a** Synthesized beampatterns in example 4; **b** Energy distribution in the spatial–spectral domain under the proposed SA with unit-PVPR constraint; **c** Normalized waveform amplitude distribution and selected antenna locations of the proposed SA

synthesized spatial-spectral energy distribution of the proposed SA. It can be clearly seen that two deep spectral notches close to − 50 dB are formed in the specific stopband regions where the two communication devices exist, which shows that the interferences caused by the transmit energy from radar can still be effectively and sufficiently suppressed, in turn manifesting the spectral compatibility of the proposed scheme. Figure 11c plots the uniform waveform amplitudes per antenna and there are 5 antennas with zero amplitudes, which implies that these five antennas are unselected.

6 Conclusion

In this paper, we proposed a switchable individual antenna power control scheme, namely SIAPC together with the novel PVPR constraint, to control the transmit power uniformity per antenna and jointly design the sparse MIMO array transceiver by antenna selection. The proposed scheme possessed more waveform designate DoFs to achieve a lower SLL than that of the common CM in the case of uniform elemental power and form multiple deeper nulls in the spatial-spectral domain in order to spectrally coexist with communications and reduce the mutual interferences between radar and communications. Numerical experiments verified the effectiveness and superiority of the proposed method compared with other methods in terms of obtaining the lower sidelobe level and deeper spectral nulls using a smallest number of antennas.

Appendix A: Proof of theorem 1

Since $\lim_{t\to\infty} \boldsymbol{u}_p^{t+1} - \boldsymbol{u}_p^t = \mathbf{0}$, along with the dual ascent step in Step3, we then have that,

$$\lim_{t\to\infty} \hat{\boldsymbol{A}}_p^H \boldsymbol{x}^{t+1} - \boldsymbol{v}_p^{t+1} = \mathbf{0}, p = 1, \ldots, P. \tag{48}$$

Moreover, since PVPR constraint is a closed and bounded set, the sequence $\{\boldsymbol{x}^t\}$ is also bounded. Meanwhile, observing that,

$$\|\boldsymbol{v}_p^t\|_2 \leq \|\hat{\boldsymbol{A}}_p^H \boldsymbol{x}^t - \boldsymbol{v}_p^t\|_2 + \|\boldsymbol{v}_p^t\|_2, \tag{49}$$

and $\boldsymbol{v}_p^t$ is constrained in the double-sided constraint in (40), thus it implies that $\{\boldsymbol{v}_p^t, \eta^t\}$ is also bounded. Hence, there exists a stationary point $\{\boldsymbol{x}^\star, \boldsymbol{v}_p^\star, \eta^\star\}$ such that

$$\lim_{t\to\infty} \boldsymbol{x}^t = \boldsymbol{x}^\star, \lim_{t\to\infty} \boldsymbol{v}_p^t = \boldsymbol{v}_p^\star, \lim_{t\to\infty} \boldsymbol{\eta}^t = \boldsymbol{\eta}^\star. \tag{50}$$

Recalling the boundedness of the augmented Lagrangian function $\mathcal{L}_\rho(\boldsymbol{x}, \eta, \boldsymbol{v}_p, \boldsymbol{u}_p)$, we then have,

$$\lim_{t\to\infty} \mathcal{L}_\rho(\boldsymbol{x}^t, \eta^t, \boldsymbol{v}_p^t, \boldsymbol{u}_p^t) = \mathcal{L}_\rho(\boldsymbol{x}^\star, \eta^\star, \boldsymbol{v}_p^\star, \boldsymbol{u}_p^\star), \tag{51}$$

which implies that

$$\begin{aligned}&\lim_{t\to\infty}\hat{\boldsymbol{A}}_p^H\boldsymbol{x}^{t+1}-\boldsymbol{v}_p^{t+1}=\hat{\boldsymbol{A}}_p^H\boldsymbol{x}^\star-\boldsymbol{v}_p^\star=\boldsymbol{0},\\&\lim_{t\to\infty}\boldsymbol{u}_p^t=\boldsymbol{u}_p^\star,\end{aligned}\tag{52}$$

for $p=1,\ldots,P$, and the limit point $\{\boldsymbol{x}^\star,\boldsymbol{v}_p^\star,\eta^\star\}$ is an optimal solution. The proof is complete.

Abbreviations

ADMM	Alternating direction method of multipliers
CA	Cyclic algorithm
CM	Constant modulus
DoFs	Degrees of freedom
DP	Dynamic programming
EC	Energy constraint
ESD	Energy spectral density
MM	Majorization-minimization
MIMO	Multiple-input-multiple-output
MSE	Maximal square error
PAR	Peak-to-average-power ratio
PA	Power amplifier
PSL	Peak sidelobe level
PVPR	Peak-to-valley-power-ratio
RF	Radio frequency
RM	Reconfigured method
SA	Sparse array
SE	Square error
SINR	Signal-to-interference-plus-noise ratio
SIAPC	Switchable individual antenna power control
SLL	Sidelobe level
SDQP	SemiDefinite quadratic programming
ULA	Uniform linear array
WCM	Waveform covariance matrix

Acknowledgements
This work was supported by the National Science Foundation of China under Grants Nos. 62071021 and 61827901, and sponsored by Beijing Nova Program.

Authors' contributions
All authors read and approved the final manuscript.

Availability of data and materials
Research data are not shared.

Declarations

Competing interests
The authors declare that they have no competing interests.

Received: 17 August 2022 Accepted: 24 November 2022
Published online: 31 December 2022

References

1. H. Griffiths, L. Cohen, S. Watts, E. Mokole, C. Baker, M. Wicks, S. Blunt, Radar spectrum engineering and management: technical and regulatory issues. Proc. IEEE **103**(1), 85–102 (2015)
2. A. Aubry, A. De Maio, M. Piezzo, A. Farina, Radar waveform design in a spectrally crowded environment via nonconvex quadratic optimization. IEEE Trans. Aerosp. Electron. Syst. **50**(2), 1138–1152 (2014)
3. A. Aubry, V. Carotenuto, A. De Maio, A. Farina, L. Pallotta, Optimization theory-based radar waveform design for spectrally dense environments. IEEE Aerosp. Electron. Syst. Mag. **31**(12), 14–25 (2016)
4. H. Leong, B. Sawe, *Channel availability for east coast high frequency surface wave radar systems* (Technical report, Defence Research Establishment Ottawa (Ontario), 2001)
5. B. Tang, J. Li, Spectrally constrained MIMO radar waveform design based on mutual information. IEEE Trans. Sign. Process. **67**(3), 821–834 (2019). https://doi.org/10.1109/TSP.2018.2887186
6. X. Zhang, X. Wang, Waveform design with controllable modulus dynamic range under spectral constraints. Sign. Process. **189**, 108285 (2021)

7. G. Cui, H. Li, M. Rangaswamy, MIMO radar waveform design with constant modulus and similarity constraints. IEEE Trans. Sign. Process. **62**(2), 343–353 (2014). https://doi.org/10.1109/TSP.2013.2288086
8. E. Raei, M. Alaee-Kerahroodi, M.R. Bhavani Shankar, ADMM based transmit waveform and receive filter design in cognitive radar systems. In: 2020 IEEE radar conference (RadarConf20), pp. 1–6 (2020). https://doi.org/10.1109/RadarConf2043947.2020.9266386
9. O. Aldayel, V. Monga, M. Rangaswamy, Successive QCQP refinement for MIMO radar waveform design under practical constraints. IEEE Trans. Sign. Process. **64**(14), 3760–3774 (2016). https://doi.org/10.1109/TSP.2016.2552501
10. X. Yu, G. Cui, M. Piezzo, S. Iommelli, L. Kong, Robust constrained waveform design for MIMO radar with uncertain steering vectors. EURASIP J. Adv. Sign. Process. **2017**(1), 1–11 (2017)
11. H. Xu, R.S. Blum, J. Wang, J. Yuan, Colocated MIMO radar waveform design for transmit beampattern formation. IEEE Trans. Aerosp. Electron. Syst. **51**(2), 1558–1568 (2015). https://doi.org/10.1109/TAES.2014.140249
12. T. Aittomaki, V. Koivunen, Low-complexity method for transmit beamforming in MIMO radars. In: 2007 IEEE international conference on acoustics, speech and signal processing—ICASSP '07, vol. 2, pp. 305–308 (2007). https://doi.org/10.1109/ICASSP.2007.366233
13. P. Stoica, J. Li, Y. Xie, On probing signal design for MIMO radar. IEEE Trans. Sign. Process. **55**(8), 4151–4161 (2007). https://doi.org/10.1109/TSP.2007.894398
14. P. Stoica, J. Li, X. Zhu, Waveform synthesis for diversity-based transmit beampattern design. IEEE Trans. Sign. Process. **56**(6), 2593–2598 (2008). https://doi.org/10.1109/TSP.2007.916139
15. D.R. Fuhrmann, G. San Antonio, Transmit beamforming for MIMO radar systems using signal cross-correlation. IEEE Trans. Aerosp. Electron. Syst. **44**(1), 171–186 (2008). https://doi.org/10.1109/TAES.2008.4516997
16. J. Lipor, S. Ahmed, M.S. Alouini, Fourier-based transmit beampattern design using MIMO radar. IEEE Trans. Sign. Process. **62**(9), 2226–2235 (2014). https://doi.org/10.1109/TSP.2014.2307838
17. G. Hua, S.S. Abeysekera, MIMO radar transmit beampattern design with ripple and transition band control. IEEE Trans. Sign. Process. **61**(11), 2963–2974 (2013). https://doi.org/10.1109/TSP.2013.2252173
18. A. Aubry, A. De Maio, Y. Huang, MIMO radar beampattern design via PSL/ISL optimization. IEEE Trans. Sign. Process. **64**(15), 3955–3967 (2016). https://doi.org/10.1109/TSP.2016.2543207
19. M.M. Naghsh, E.H.M. Alian, M.M. Hashemi, M.M. Nayebi, Cognitive MIMO radars: an information theoretic constrained code design method. In: 2016 24th European signal processing conference (EUSIPCO), pp. 2215–2219 (2016). https://doi.org/10.1109/EUSIPCO.2016.7760642
20. B. Tang, J. Li, Spectrally constrained MIMO radar waveform design based on mutual information. IEEE Trans. Sign. Process. **67**(3), 821–834 (2019). https://doi.org/10.1109/TSP.2018.2887186
21. M. Arulraj, S.J. Thiruvengadam, MIMO radar waveform design with peak and sum power constraints. EURASIP J. Adv. Sign. Process. **2013**(1), 1–12 (2013)
22. Z. Cheng, Z. He, S. Zhang, J. Li, Constant modulus waveform design for MIMO radar transmit beampattern. IEEE Trans. Sign. Process. **65**(18), 4912–4923 (2017). https://doi.org/10.1109/TSP.2017.2718976
23. S. Boyd, N. Parikh, E. Chu, B. Peleato, J. Eckstein, Distributed optimization and statistical learning via the alternating direction method of multipliers. Found. Trends® Mach. Learn. **3**(1), 1–122 (2011)
24. Z. Zhao, D.P. Palomar, MIMO transmit beampattern matching under waveform constraints. In: 2018 IEEE international conference on acoustics, speech and signal processing (ICASSP), pp. 3281–3285 (2018). https://doi.org/10.1109/ICASSP.2018.8462047
25. Y. Sun, P. Babu, D.P. Palomar, Majorization-minimization algorithms in signal processing, communications, and machine learning. IEEE Trans. Sign. Process. **65**(3), 794–816 (2017). https://doi.org/10.1109/TSP.2016.2601299
26. W. Fan, J. Liang, J. Li, Constant modulus MIMO radar waveform design with minimum peak sidelobe transmit beampattern. IEEE Trans. Sign. Process. **66**(16), 4207–4222 (2018). https://doi.org/10.1109/TSP.2018.2847636
27. X. Zhang, X. Wang, MIMO radar waveform design with desirable beampattern and controllable power uniformity. In: 2021 international conference on control, automation and information sciences (ICCAIS), pp. 392–397 (2021). https://doi.org/10.1109/ICCAIS52680.2021.9624505
28. X. Wang, W. Li, V.C. Chen, Hand Gesture Recognition Using Radial and Transversal Dual Micromotion Features. IEEE Trans. Aerosp. Electron. Syst. **58**(6), 5963–5973 (2022). https://doi.org/10.1109/TAES.2022.3179679
29. X. Zhang, J. Liang, X. Fan, G. Yu, H.C. So, Reconfigurable array beampattern synthesis via conceptual sensor network modeling and computation. IEEE Trans Antennas Propag **68**(6), 4512–4525 (2020). https://doi.org/10.1109/TAP.2020.2972401
30. W. Zhai, X. Wang, M.S. Greco, F. Gini, Joint optimization of sparse FDAs for time invariant transmit beampattern synthesis. IEEE Sign. Process. Lett. **29**, 110–114 (2022). https://doi.org/10.1109/LSP.2021.3128317
31. Y. Aslan, J. Puskely, J.H.J. Janssen, M. Geurts, A. Roederer, A. Yarovoy, Thermal-aware synthesis of 5G base station antenna arrays: An overview and a sparsity-based approach. IEEE Access **6**, 58868–58882 (2018). https://doi.org/10.1109/ACCESS.2018.2873977
32. N. Amani, A. Farsaei, S.R. Aghdam, T. Eriksson, M.V. Ivashina, R. Maaskant, Sparse array synthesis including mutual coupling for mu-mimo average capacity maximization. IEEE Trans. Antennas Propag. **70**(8), 6617–6626 (2022). https://doi.org/10.1109/TAP.2022.3177450
33. X. Wang, W. Zhai, M. Greco, F. Gini, Cognitive sparse beamformer design in dynamic environment via regularized switching network. IEEE Trans. Aerosp. Electron. Syst. (2022). https://doi.org/10.1109/TAES.2022.3207706
34. Z. Cheng, Y. Lu, Z. He, Yufengli, J. Li, X. Luo, Joint optimization of covariance matrix and antenna position for MIMO radar transmit beampattern matching design. In: 2018 IEEE radar conference (RadarConf18), pp. 1073–1077 (2018). https://doi.org/10.1109/RADAR.2018.8378710
35. A. Bose, S. Khobahi, M. Soltanalian, Efficient waveform covariance matrix design and antenna selection for MIMO radar. Sign. Process. **183**, 107985 (2021)
36. E.K. Ghafi, S.A. Ghorashi, E. Mehrshahi, Reconfigurable linear antenna arrays for beam-pattern matching in collocated MIMO radars. IEEE Trans. Aerosp. Electron. Syst. **57**(5), 2715–2724 (2021)
37. X. Wang, M.S. Greco, F. Gini, Adaptive sparse array beamformer design by regularized complementary antenna switching. IEEE Trans. Sign. Process. **69**, 2302–2315 (2021). https://doi.org/10.1109/TSP.2021.3064183

38. Z. Cheng, Z. He, B. Liao, M. Fang, MIMO radar waveform design with PAPR and similarity constraints. IEEE Trans. Sign. Process. **66**(4), 968–981 (2018). https://doi.org/10.1109/TSP.2017.2780052
39. X. Zhang, X. Wang, Waveform design with controllable modulus dynamic range under spectral constraints. Sign. Process. **189**, 108285 (2021)
40. A. Aubry, A. De Maio, M. Piezzo, M.M. Naghsh, M. Soltanalian, P. Stoica, Cognitive radar waveform design for spectral coexistence in signal-dependent interference. In: 2014 IEEE radar conference, pp. 0474–0478 (2014)
41. A. Aubry, A. De Maio, M. Piezzo, A. Farina, Radar waveform design in a spectrally crowded environment via nonconvex quadratic optimization. IEEE Trans. Aerosp. Electron. Syst. **50**(2), 1138–1152 (2014). https://doi.org/10.1109/TAES.2014.120731
42. Z. Cheng, C. Han, B. Liao, Z. He, J. Li, Communication-aware waveform design for MIMO radar with good transmit beampattern. IEEE Trans. Sign. Process. **66**(21), 5549–5562 (2018). https://doi.org/10.1109/TSP.2018.2868042
43. H. Griffiths, L. Cohen, S. Watts, E. Mokole, C. Baker, M. Wicks, S. Blunt, Radar spectrum engineering and management: technical and regulatory issues. Proc. IEEE **103**(1), 85–102 (2015). https://doi.org/10.1109/JPROC.2014.2365517
44. J. Li, P. Stoica, *MIMO Radar Signal Processing* (Wiley, New York, 2008), pp.1–448. https://doi.org/10.1002/9780470391488
45. J. Song, P. Babu, D.P. Palomar, Optimization methods for designing sequences with low autocorrelation sidelobes. IEEE Trans. Sign. Process. **63**(15), 3998–4009 (2015). https://doi.org/10.1109/TSP.2015.2425808
46. R. Vescovo, Consistency of constraints on nulls and on dynamic range ratio in pattern synthesis for antenna arrays. IEEE Trans. Antennas Propag. **55**(10), 2662–2670 (2007). https://doi.org/10.1109/TAP.2007.905828
47. J. Eckstein, D.P. Bertsekas, On the Douglas–Rachford splitting method and the proximal point algorithm for maximal monotone operators. Math. Program. **55**(3), 293–318 (1992)
48. Z. Wen, Y. Chao, L. Xin, S. Marchesini, Alternating direction methods for classical and ptychographic phase retrieval. Inverse Probl. **28**(11), 115010 (2012)
49. Z.F. Cheng, Y.B. Zhao, H. Li, P.L. Shui, Sparse representation framework for MIMO radar transmit beampattern matching design. IEEE Trans. Aerosp. Electron. Syst. **53**(1), 520–529 (2017). https://doi.org/10.1109/TAES.2017.2650739

Publisher's Note